Effect of magnon-magnon interaction on ferromagnetism in hexagonal manganese pnictide monolayers

S. Memarzadeh,[1,*] R. Caglayan,[2,*] Y. Mogulkoc,[3] M. Modarresi,[1,†] and A. Mogulkoc[2]
[1]*Department of Physics, Faculty of Science, Ferdowsi University of Mashhad, Mashhad, Iran*
[2]*Department of Physics, Faculty of Sciences, Ankara University, 06100 Tandogan, Ankara, Turkey*
[3]*Department of Physics Engineering, Faculty of Engineering, Ankara University, 06100 Tandogan, Ankara, Turkey*

(Received 12 June 2022; revised 25 December 2022; accepted 14 March 2023; published 6 April 2023)

We have studied the finite-temperature magnetic phase transition using a combination of first-principles calculations and the second-order Holstein-Primakoff approximation of the anisotropic Heisenberg model for hexagonal MnX (X = N, P, As, and Sb) monolayers. The MnX monolayers are all half-metal with dynamically and thermally stable atomic structures at T = 300 K. The hexagonal MnN is an out-of-plane easy-axis ferromagnetically ordered monolayer with the Curie temperature close to the room temperature. However, the other three MnX (X = P, As, and Sb) monolayers have an easy axis inside the plane with Curie temperature close to zero. The *ab initio* energy difference between spin configurations is mapped into an anisotropic Heisenberg spin Hamiltonian which is solved using the second-order Holstein-Primakoff approximation. The anharmonic (magnon-magnon) interaction softens the magnetic excitation energy and reduces the magnon energy gap at the Γ point, which is crucial for the finite-temperature long-range magnetic order in two dimensions. As a result, the inclusion of magnon-magnon interaction dramatically reduces the Curie temperature of hexagonal MnX monolayers. Although the magnon-magnon interaction is a perturbation in energy dispersion, it has an important effect on the finite-temperature long-range magnetic order in two-dimensional monolayers.

DOI: 10.1103/PhysRevB.107.144409

I. INTRODUCTION

The recent discovery of two-dimensional (2D) magnetic materials has gained considerable attention in recent years [1–7]. There are various synthesized and theoretically studied 2D ferromagnetic monolayers [1,6,8–18]. According to experimental observations, most ferromagnetic monolayers have low Curie temperatures [1,13–17,19], while various 2D magnets have been predicted with Curie temperatures well above the room temperature [20–27]. There are also various experimental reports of room-temperature ferromagnetic monolayers [11,18,28–31]. The large difference in the observed Curie temperature of monolayers can be attributed to the value of exchange between magnetic moments. For 2D monolayers, according to the Mermin-Wagner-Hohenberg theorem [32,33], the magnetic anisotropy is crucial to stabilize long-range magnetic order at any finite temperature. The role of magnetic anisotropy is to open an energy gap inside the magnon spectrum and limits the number of excited magnons at a finite temperature. However, the thermal fluctuation may close the magnon gap and annihilate magnetic order at low temperatures.

In most of the previous theoretical works, the thermodynamics of 2D monolayers is studied by using the mean-field approximation [34,35], the classical Monte Carlo simulation based on the Ising spin model [36,37], the random-phase approximation [34,35], or the first-order Holstein-Primakoff (HP) approximation [10,38,39]. The well-known Bloch's spin-wave theory disregards the magnon-magnon interaction [40]. At sufficiently low temperatures, the average number of thermally flipped spins meaningfully vanish, which hypothetically reduces interaction. As a result, the spin excited states are well described as zero-temperature magnon dispersion energy. However, the physics of excited states at high temperatures close to the phase transition is strongly affected by the magnon-magnon interaction [41–43].

The magnetic anisotropy energy opens an energy gap in the magnon spectrum, which limits the number of excited magnons. The value of magnetic anisotropy and the resultant magnon energy gap are generally small. The interplay of magnetic anisotropy and magnon-magnon interaction in the formation of the long-range 2D magnetic order and the value of Curie temperature is still not well understood. The origin of finite-temperature 2D magnetism is more complex than the simple noninteracting magnon picture and deserves a deeper theoretical study. Here we study the electronic and magnetic structure of all MnX (X = N, P, As, and Sb) monolayers within the combination of DFT+U and the anisotropic Heisenberg model. We address the magnon energy normalization and magnetic phase transitions by the inclusion of magnon-magnon interaction within the second-order HP approximation. The magnon spectra correction is carried out by using the Hartree-Fock approximation and a self-consistent solution of energy. As a result, we calculate the temperature-dependent magnon energy correction in the first Brillouin zone for hexagonal MnX monolayers. Finally, we show that the magnon-magnon interaction dramatically reduces the Curie temperature in the 2D MnX monolayers. The rest of the

*These authors contributed equally to this work.
†m.modarresi@um.ac.ir

paper is organized as follows. Sec. II provides computational details and theoretical methods for the anisotropic Heisenberg model. In Sec. III A, we investigate the atomic and electronic structure and stability of the MnX monolayers. The thermal evaluation of the magnon energy spectrum and long-range magnetization in the second-order HP approximation is discussed in Sec. III B. We briefly summarize our findings and conclude the paper in Sec. IV.

II. MODEL AND METHOD

A. First-principles calculations

The first-principles calculations based on density-functional theory (DFT) are performed using the projected augmented wave [44,45] method as utilized in the Vienna *Ab initio* Simulation Package (VASP) [46,47]. The generalized gradient approximation based on the Perdew-Burke-Ernzerhof [48] functional is employed to describe the exchange-correlation functional. The plane-wave basis set's cutoff energy is set to 800 eV. The integration of the Brillouin zone is performed with a (32×32×1) k-point mesh by using the gamma-centered Monkhorst-Pack algorithm [49]. The lattice constants and atomic positions are optimized by the conjugate gradient method, with a maximum Hellmann-Feynman force of 0.001 eV Å^{-1} on each atom. The energy convergence criterion between consecutive steps is taken to be 10^{-10} eV. The vacuum layer along the z direction to prevent interactions between adjacent images is set to 30 Å. The effects of strongly correlated electrons in atomic d orbitals are described with the DFT+U method [50,51] by utilizing the effective on-site Coulomb repulsion to the d orbitals of Mn atoms. The value of the effective Hubbard-U parameter depends on the chemical structure and can be modulated by substrate dielectric screening and environmental effects. We have obtained the values of the U parameters of all MnX (X = N, P, As, and Sb) structures with the linear response approach proposed by Cococcioni and Gironcoli [52]. The dynamical stability was examined with phonon spectra by using the PHONOPY [53] code based on density-functional perturbation theory. All phonon calculations are performed in a 4×4×1 supercell. The thermal stability of all MnX monolayers is further examined by using the *ab initio* molecular dynamics calculations in a canonical ensemble with the Anderson thermostat. The system is considered as a 4×4×1 supercell, and the total simulation time is 2 ps with a 1-fs time interval at 300 K. Additionally, the Bader charge analysis is used to examine the bonding nature between Mn and pnictogen atoms [54–56].

B. Anisotropic Heisenberg spin model

1. In-plane easy axis

The spin model is considered as the anisotropic Heisenberg Hamiltonian,

$$H = -\frac{J}{2}\sum_{\langle ij\rangle}\mathbf{S}_i\cdot\mathbf{S}_j - \frac{\Gamma}{2}\sum_{\langle ij\rangle}\left(S_i^xS_j^y + S_i^yS_j^x\right) - \frac{\delta}{2}\sum_{\langle ij\rangle}S_i^zS_j^z - A\sum_i\left(S_i^z\right)^2. \quad (1)$$

The first term denotes the isotropic Heisenberg exchange $J_{ij} = J_{ji} = J$ with summation over the nearest-neighbor pairs of atoms $\langle ij\rangle$. The 1/2 factor is to avoid double-counting of the pairs. The $J > 0$ ($J < 0$) is corresponding to the ferromagnetic (antiferromagnetic) coupling between nearest-neighbor moments. The nearest-neighbor exchange interaction approximation for the localized magnetic moments is widely used for the description of 2D magnetic monolayers [57–61]. The next three terms describe the in-/out-of-plane magnetic anisotropy. The second term describes the intersite magnetic anisotropy within the xy plane (monolayer plane), where the Γ term is the corresponding interaction parameter. The Γ parameter defines an easy axis in the Cartesian basis for the hexagonal lattice [62,63]. The third term describes the out-of-plane magnetic anisotropy, where δ is the diagonal zz component of the intersite magnetic anisotropy tensor and the last term is the single-ion magnetic anisotropy energy. The positive values of A and δ correspond to the out-of-plane easy axis while for negative A and δ the easy axis lies inside the xy plane. In fact, the magnetic order in 2D monolayers is achieved by breaking the symmetry usually provided by the inherent magnetic anisotropy [10,38].

The anisotropic Heisenberg spin model can be transformed to a bosonic Hamiltonian via the in-plane HP transformations [64],

$$S_i^+ = a_i^\dagger\sqrt{2S - a_i^\dagger a_i},$$
$$S_i^- = \sqrt{2S - a_i^\dagger a_i}\,a_i,$$
$$S_i^x = a_i^\dagger a_i - S, \quad (2)$$

where S is the total angular momentum of a spin and $S_i^\pm = -S_i^z \pm iS_i^y$ are spin ladder operators.

The spin operators can be expanded in the first-order HP transformation [10,38,39,65]. This approximation is based on the low number of excited magnons, which is not appropriate to describe the magnetic phase transition at higher temperatures. To describe the magnon at a higher temperature, we consider the second-order HP transformation for the spin operators. In the second-order HP approximation, the leader operators are expanded as $S_i^+ \approx \sqrt{2S}(a_i^\dagger - \frac{a_i^\dagger a_i^\dagger a_i}{4S})$ and $S_i^- \approx \sqrt{2S}(a_i - \frac{a_i^\dagger a_i a_i}{4S})$. By substituting the expansion of ladder operators into the spin Hamiltonian, the transformed bosonic Hamiltonian consists of noninteracting and anharmonic magnon-magnon two-particle interactions (see Appendix B 1 for details) [41,66].

By applying the Hartree-Fock decoupling to the interacting bosonic Hamiltonian [Eq. (B3)], and diagonalization of the final bosonic Hamiltonian, $H = \sum_{\mathbf{k}}\beta_{\mathbf{k}}a_{\mathbf{k}}^\dagger a_{\mathbf{k}} + \sum_{\mathbf{k}}\alpha_{\mathbf{k}}a_{\mathbf{k}}^\dagger a_{-\mathbf{k}}^\dagger + \sum_{\mathbf{k}}\alpha_{\mathbf{k}}a_{\mathbf{k}}a_{-\mathbf{k}}$ [Eq. (B4)], the interacting magnon energy becomes

$$E_{\mathbf{k}} = \sqrt{(\beta_{\mathbf{k}})^2 - 4(\alpha_{\mathbf{k}})^2}, \quad (3)$$

where $\beta_{\mathbf{k}} = \hbar\omega_{\mathbf{k}} + \Delta$,

$$\hbar\omega_{\mathbf{k}} = \hbar\omega_{\mathbf{k}}^0 + \hbar\omega_{\mathbf{k}}^T = \sum_{\Delta\mathbf{R}} S\left(\frac{2J-\Gamma+\delta}{2}\right)(1-\cos(\mathbf{k}\cdot\Delta\mathbf{R}))\left(1-\frac{1}{NS}\sum_{\mathbf{k}'} n_{\mathbf{k}'}\left[1-\frac{2(J+\Gamma)}{2J-\Gamma+\delta}\cos(\mathbf{k}'\cdot\Delta\mathbf{R})\right]\right), \quad (4)$$

$$\Delta = \Delta^0 + \Delta^T = \left((3\Gamma-\delta)\frac{SZ}{2} - AS\right) - \sum_{\mathbf{k}'} n_{\mathbf{k}'}\left(\frac{(3\Gamma-\delta)Z-4A}{2N} + \frac{3\Gamma-\delta}{2N}\sum_{\Delta\mathbf{R}}\cos(\mathbf{k}'\cdot\Delta\mathbf{R})\right), \quad (5)$$

and

$$\alpha_{\mathbf{k}} = \alpha_{\mathbf{k}}^0 + \alpha_{\mathbf{k}}^T = \left(-\frac{A}{2}S - \frac{S}{4}(\Gamma+\delta)\sum_{\Delta\mathbf{R}}\cos(\mathbf{k}\cdot\Delta\mathbf{R})\right) + \left(\sum_{\mathbf{k}'} n_{\mathbf{k}'}\left[3\frac{A}{4N} + \frac{\Gamma+\delta}{8N}\left(2\sum_{\Delta\mathbf{R}}\cos(\mathbf{k}\cdot\Delta\mathbf{R}) + \sum_{\Delta\mathbf{R}}\cos(\mathbf{k}'\cdot\Delta\mathbf{R})\right)\right]\right). \quad (6)$$

Here Z is the number of nearest neighbors and $\langle a_{\mathbf{k}}^\dagger a_{\mathbf{k}'}\rangle = \delta_{\mathbf{k},\mathbf{k}'} n_{\mathbf{k}}$. The three terms,

$$\hbar\omega_{\mathbf{k}}^0 = S\left(\frac{2J-\Gamma+\delta}{2}\right)\sum_{\Delta\mathbf{R}}[1-\cos(\mathbf{k}\cdot\Delta\mathbf{R})],$$
$$\Delta^0 = \left((3\Gamma-\delta)\frac{SZ}{2} - AS\right), \quad \text{and}$$
$$\alpha_{\mathbf{k}}^0 = \left(-\frac{A}{2}S - \frac{S}{4}(\Gamma+\delta)\sum_{\Delta\mathbf{R}}\cos(\mathbf{k}\cdot\Delta\mathbf{R})\right) \quad (7)$$

correspond to the first-order HP expansion of the magnon spectrum (see Appendix B 1). Here the $\hbar\omega_{\mathbf{k}}^T$ is the wave vector dependent magnon dispersion correction, and Δ^T is the magnon gap correction due to the magnon-magnon interaction. The value of magnon interaction correction (Δ^T) is always negative, which reduces the magnon energy gap at the Γ point. The $\alpha_{\mathbf{k}}$ is the contribution of off-diagonal parts to magnon dispersion and energy gap. The lowering of the magnon energy gap at the finite temperature reduces the critical temperature for the ferromagnetic to paramagnetic phase transition. The zero-temperature magnon energy gap in the absence of magnon-magnon interaction is derived as $E_{\mathbf{k}=\mathbf{0}}^{T=0} = S\sqrt{72\Gamma^2 - 72\delta\Gamma - 24A\Gamma}$. For 2D monolayers with easy axis inside the plane, the value of the magnon energy gap directly depends on the Γ parameter. In the case of easy-plane material with $\Gamma = 0$, the magnon energy gap disappears at finite temperature, which is consistent with the Mermin-Wagner-Hohenberg theorem.

2. Out-of-plane easy axis

The spins interaction is modeled based on the well-known Heisenberg Hamiltonian,

$$H = -\frac{J}{2}\sum_{\langle ij\rangle}\mathbf{S}_i\cdot\mathbf{S}_j - \frac{\delta}{2}\sum_{\langle ij\rangle}S_i^z S_j^z - A\sum_i\left(S_i^z\right)^2. \quad (8)$$

Using the HP theory for out-of-plane easy axis defined as

$$S_i^+ = \sqrt{2S - a_i^\dagger a_i}\,a_i,$$
$$S_i^- = a_i^\dagger\sqrt{2S - a_i^\dagger a_i},$$
$$S_i^z = S - a_i^\dagger a_i, \quad (9)$$

where $S^\pm = S^x \pm iS^y$ are spin ladder operators, magnon energy takes the form

$$\hbar\omega_{\mathbf{k}} = \hbar\omega_{\mathbf{k}}^0 + \hbar\omega_{\mathbf{k}}^T = SJ\sum_{\Delta\mathbf{R}}(1-\cos(\mathbf{k}\cdot\Delta\mathbf{R})) \times\left[1-\frac{1}{NS}\sum_{\mathbf{k}'}\left(1-\frac{(J+\delta)}{J}\cos(\mathbf{k}'\cdot\Delta\mathbf{R})\right)n_{\mathbf{k}'}\right] \quad (10)$$

and

$$\Delta = \Delta^0 + \Delta^T = (A(2S-1) + S\delta Z) - \left(\frac{(\delta Z+4A)}{N}\sum_{\mathbf{k}'} n_{\mathbf{k}'} + \frac{\delta}{N}\sum_{\Delta\mathbf{R}}\sum_{\mathbf{k}'}(\cos(\mathbf{k}'\cdot\Delta\mathbf{R}))n_{\mathbf{k}'}\right). \quad (11)$$

See Appendix B 2 for more details.

C. Temperature-dependent magnetization

In the thermodynamic limit, each excited magnon reduces total spin by one unit. As a result, the total magnetization at a finite temperature can be obtained by counting the number of excited magnons,

$$\frac{M(T)}{M_{\text{sat}}} = 1 - \frac{1}{S}\sum_{\mathbf{k}}\frac{1}{\exp(\beta E_{\mathbf{k}}) - 1}. \quad (12)$$

Here M_{sat} is the saturation magnetization. For the zero magnon energy gap at a finite temperature, there will be an infinite number of excited magnons at the Γ point and $M(T>0)$ goes to zero, in agreement with the Mermin-Wagner-Hohenberg theorem. Therefore, the anisotropy energy gap at the Γ is essential to preserve the 2D long-range magnetic order at a finite temperature.

III. RESULTS AND DISCUSSION

A. Atomic and electronic configuration

We first consider the hexagonal MnX (X = N, P, As, and Sb) monolayers unit cell as shown from the top and side view in Fig. 1. The lattice parameters of MnN, MnP, MnAs, and

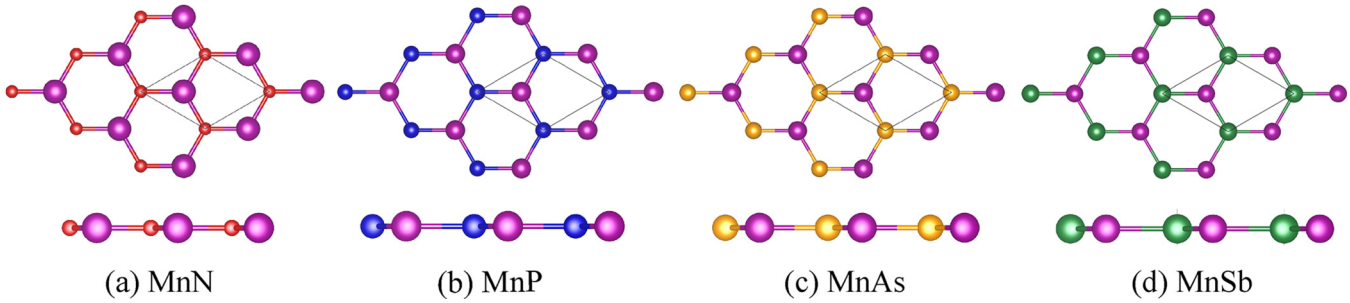

FIG. 1. Top and side views of (a) MnN, (b) MnP, (c) MnAs, and (d) MnSb monolayers.

MnSb hexagonal monolayers are equal to 3.37, 4.20, 4.35, and 4.74 Å, respectively, as presented in Table I. These results are comparable with previous studies of hexagonal MnN [67,68]. The Hubbard (U) parameter is determined by using the linear response theory as mentioned in Sec. II A. The corresponding converged Hubbard U values of MnX monolayers are presented in Fig. S1 (see Supplemental Material [69]). Our findings are compatible with previous monolayer MnX studies [67,68,70]. On the other hand, we observe that Hubbard U parameters of MnX monolayers depend on the pnictogen atoms. Also, we notice that the dimension of the materials can affect the Hubbard parameter [71–74], e.g., the Hubbard parameter of monolayer MnAs (see Table I) is increased by a factor of ∼2 compared to the bulk MnAs crystal [74]. According to our DFT calculations, the ground state of all MnX monolayers is the ferromagnetic arrangement of spins with a net moment of $4\mu_B$ per Mn atom (corresponding to an $S = 2$ electronic system). To investigate the synthesis feasibility of MnX, we calculate the cohesive energies, $E_{\mathrm{Coh}} = E_{\mathrm{Mn}} + E_X - E_{\mathrm{Mn}X}$, where $E_{\mathrm{Mn}X}$ is the total energy of the MnX monolayer, E_{Mn} and E_X are the single-atom energies of manganese and pnictogen atoms, respectively. The high cohesive energies in Table I indicate that the manganese and pnictogen atoms are bonded tightly, thus they are suitable for synthesis [75,76]. The cohesive energies of MnX vary around 4–8 eV/atom with a similar trend to that of hexagonal CrX monolayers [8]. The absence of imaginary phonon frequencies ensures the dynamical stability of all hexagonal MnX monolayers (see Fig. S2 in the Supplemental Material). The phonon frequencies of MnX monolayers decrease with an increasing atomic mass of pnictogen atoms. Furthermore, we examine the thermodynamic stability of the MnX monolayer by utilizing the *ab initio* molecular dynamics simulations within the canonical ensemble (*NVT*) and Anderson thermostat at the room temperature ($T = 300$ K) for 2 ps. The variation of total energy during molecular dynamics and the final snapshot of atomic configurations are shown in the Supplemental Material (see Fig. S3). There is no significant atomic distortion or phase transitions due to the thermal fluctuations in MnX monolayers. These small thermal distortions become more pronounced with the decreasing atomic mass of pnictogen atoms. In Table I, we demonstrate the electron transfer from manganese to pnictogen atoms with the Bader charge analysis. The charge-transfer amount between manganese and pnictogen (from N to Sb) atoms decreases from ∼1.3 to 0.8 $|e|$ owing to the decreasing electronegativity with the increasing atomic mass. The electronegativity differences of MnN, MnP, MnAs, and MnSb are found to be 1.49, 0.64, 0.63, and 0.5 on the Pauling scale, which are correlated with charge transfers (ΔQ) and cohesive energies (E_{Coh}). All MnX monolayers are half-metal with a large electronic energy gap for the spin-down state, as shown in Fig. 2. The pure spin-up states at the Fermi level can be a perfect spin polarizer for spintronic devices. The valence edge of spin-down states arises from the hybridization of both Mn and pnictide atoms. However, the edge of the conduction band results purely from the Mn atom. We also show electronic bands in the presence of spin-orbit coupling (SOC) as dashed lines in Fig. 2. The SOC mixes electronic up and down spin states and forms spinors. According to our results, the SOC has a negligible effect on the electronic structure of MnX monolayers. The flat band close to the Fermi level can occupy a particularly large number of spin-up electrons, which leads to strong many-body interactions and exotic states of matter [77,78]. According to the partial density of states (DOS), the peak in the density of states arises from pnictogen atoms. For the MnN monolayer, the flat band and the peak in DOS cross the Fermi level.

B. Finite-temperature magnetism

We use the anisotropic Heisenberg spin Hamiltonian to study the magnetization as a function of temperature for MnX

TABLE I. The calculated value of the Hubbard U parameter in the linear response theory, lattice constant, cohesive energies, Bader electron transfer from Mn to pnictogen atom, easy axis, anisotropic Heisenberg parameters, magnon gap at $T = 0$ K (Δ^0), and Curie temperature with second-order HP (T_C) and first-order HP (T_C^1) approximations for all MnX monolayers.

	U (eV)	a (Å)	E_{Coh} (eV)	ΔQ ($\lvert e\rvert$)	Easy axis	J (meV)	A (meV)	δ (μeV)	Γ (μeV)	Δ^0 (meV)	T_C (K)	T_C^1 (K)
MnN	5.60	3.37	7.82	1.32	out of plane	12.32	0.02	1.18		0.074	480	820
MnP	5.80	4.20	5.25	0.99	in plane	7.66	−0.02	2.38	0.002	0.002	7	445
MnAs	4.90	4.35	4.70	0.90	in plane	7.36	−0.11	−24.92	0.044	0.028	18	585
MnSb	5.60	4.74	3.94	0.78	in plane	4.94	−0.38	−127.42	0.204	0.122	24	505

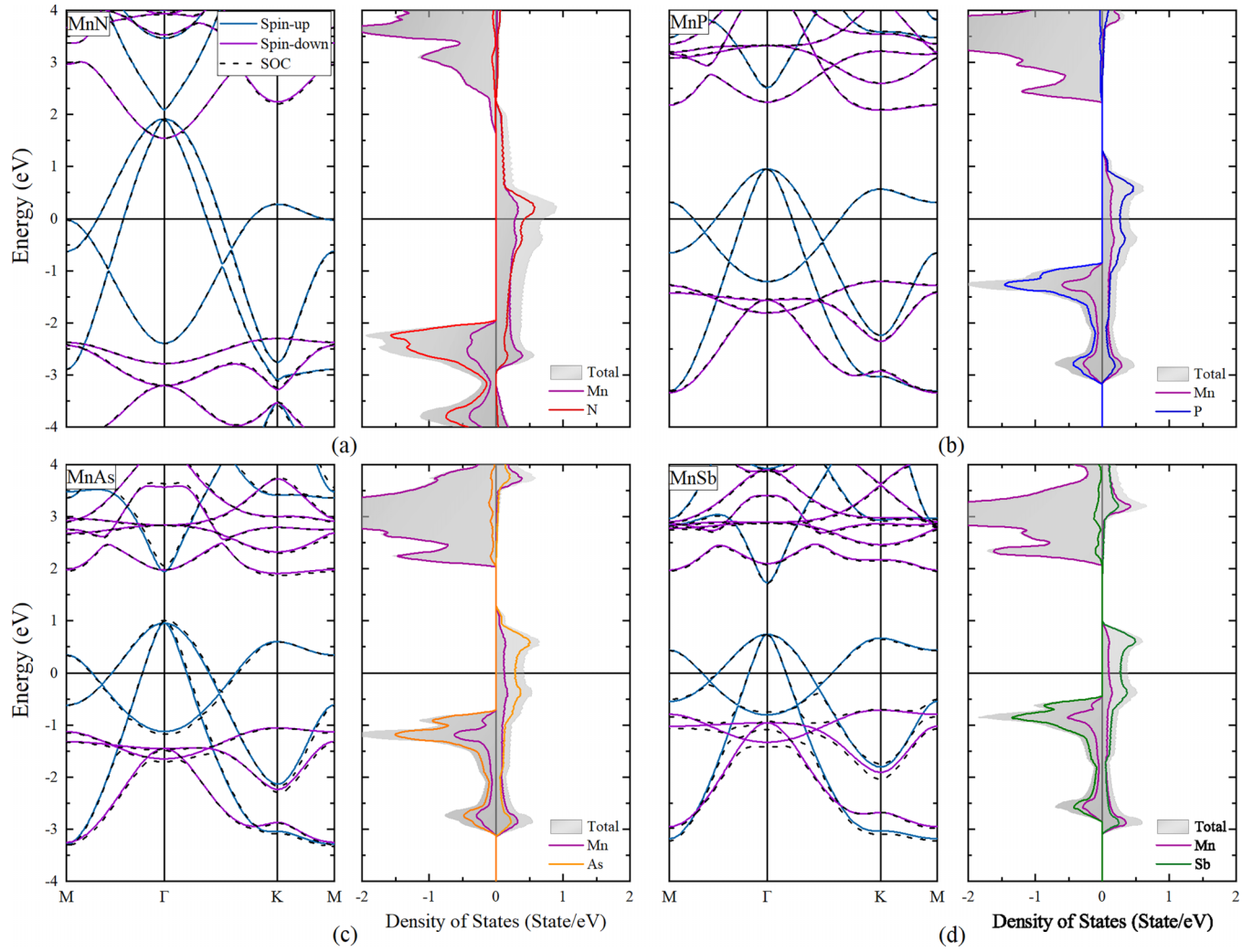

FIG. 2. The spin-polarized electronic band structure of MnX monolayers in the absence (solid line) and presence (dashed line) of spin-orbit coupling. The side figures show the total and projected density of states on the Mn and pnictogen atoms.

monolayers. The spin model parameters are derived from the energy difference between different magnetic configurations as shown in Appendix A. For hexagonal MnX monolayers, anisotropic Heisenberg Hamiltonian parameters J, Γ, A, and δ are presented in Table I. Although the effect of the SOC on the magnetic exchange interaction is negligible, we have taken the SOC into account to determine magnetic anisotropies. It is because the magnetic anisotropies, which are essential to stabilize magnetic order in 2D materials, are driven by the SOC. The easy-axis direction depends on the type of ligand atom. The MnN monolayer has an out-of-plane easy axis with a relatively strong isotropic nearest-neighbor exchange interaction. The other MnX monolayers are all in FM in-plane ground state and the value of magnetic anisotropy is increasing with the atomic mass of the ligand atom. According to our calculations, there is an easy axis inside the monolayer plane, which is characterized by the Γ parameter. The Γ parameter has a vital role to open the magnon energy gap which stabilizes the 2D structure. Accordingly, for the case of $\Gamma = 0$, the material has a magnetic easy plane with no finite-temperature long-range magnetic order [38]. The finite-temperature magnon dispersion of the hexagonal MnX monolayer is obtained from the self-consistent solution of $E_{\mathbf{k}} = \Delta + \hbar\omega_{\mathbf{k}}$. The self-consistent loop is started from the noninteracting magnon spectrum $E^0_{\mathbf{k}} = \hbar\omega^0_{\mathbf{k}} + \Delta^0$. The noninteracting magnon energies, $E^0_{\mathbf{k}}$, for hexagonal MnX monolayers are plotted along the high-symmetry point inside the first Brillouin zone in Fig. 3.

For the MnX unit cell with one spin, there is one acoustic magnon branch [79]. The magnon spectrum is softened smoothly from the MnN to the MnSb monolayer. The minimum energy at the Γ point is equal to the noninteracting gap values Δ^0, which are presented in Table I. The energy increases monotonically toward the edge of the first Brillouin zone. The magnon energy gap is generally increasing with the increasing atomic mass and the strength of spin-orbit coupling in pnictogen atoms. For example, the MnSb magnon energy gap is two orders of magnitude larger than the MnP monolayer. The energy correction due to the magnon-magnon interaction ($-\hbar\omega^T_{\mathbf{k}}$) for the MnN monolayer depends on the wave vector as shown in Fig. 4(a). By the increasing temperature, the number of excited magnons and the interaction strength are increased together. Due to the perturbative second-order term in the HP transformation expansion, the

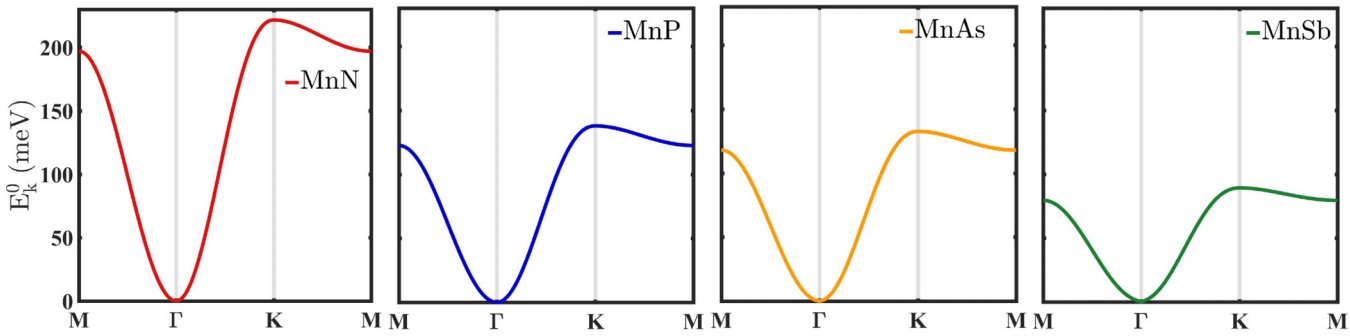

FIG. 3. The noninteracting magnon energy spectrum ($E_{\mathbf{k}}^0$) in the high- symmetry path for MnX (X = N, P, As, and Sb) monolayers.

magnon-magnon correction is negligibly small in the entire first Brillouin zone [see Fig. 4(a)] but it is critically important at the Γ point. The low-energy magnon states around the Γ point play an important role in the thermal behavior of magnetization in 2D monolayers.

The magnon energy gap modification with temperature for MnN and MnX (X = P, As, and Sb) monolayers are shown in Figs. 4(b) and 5(a), respectively. The energy gap is reducing slowly close to $T = 0$ K and sharply drops to zero. The energy gap renormalization at the Γ point is related to the magnon softening. The temperature dependence of magnetization from Eq. (12) in the second-order HP approximations are presented in Figs. 4(c) and 5(b). For the second-order HP, the finite magnetization is obtained in the self-consistent solution of the magnon spectrum in Eq. (12). We define the Curie temperature (T_C) as the point where the magnetization reduces to half of the saturation value, i.e., $M_{\text{sat}}/2$ [10]. In the second-order HP approximation, above the Curie temperature, the magnetization goes to zero very fast. Although the integral of Eq. (12) is taken throughout the first Brillouin zone, it

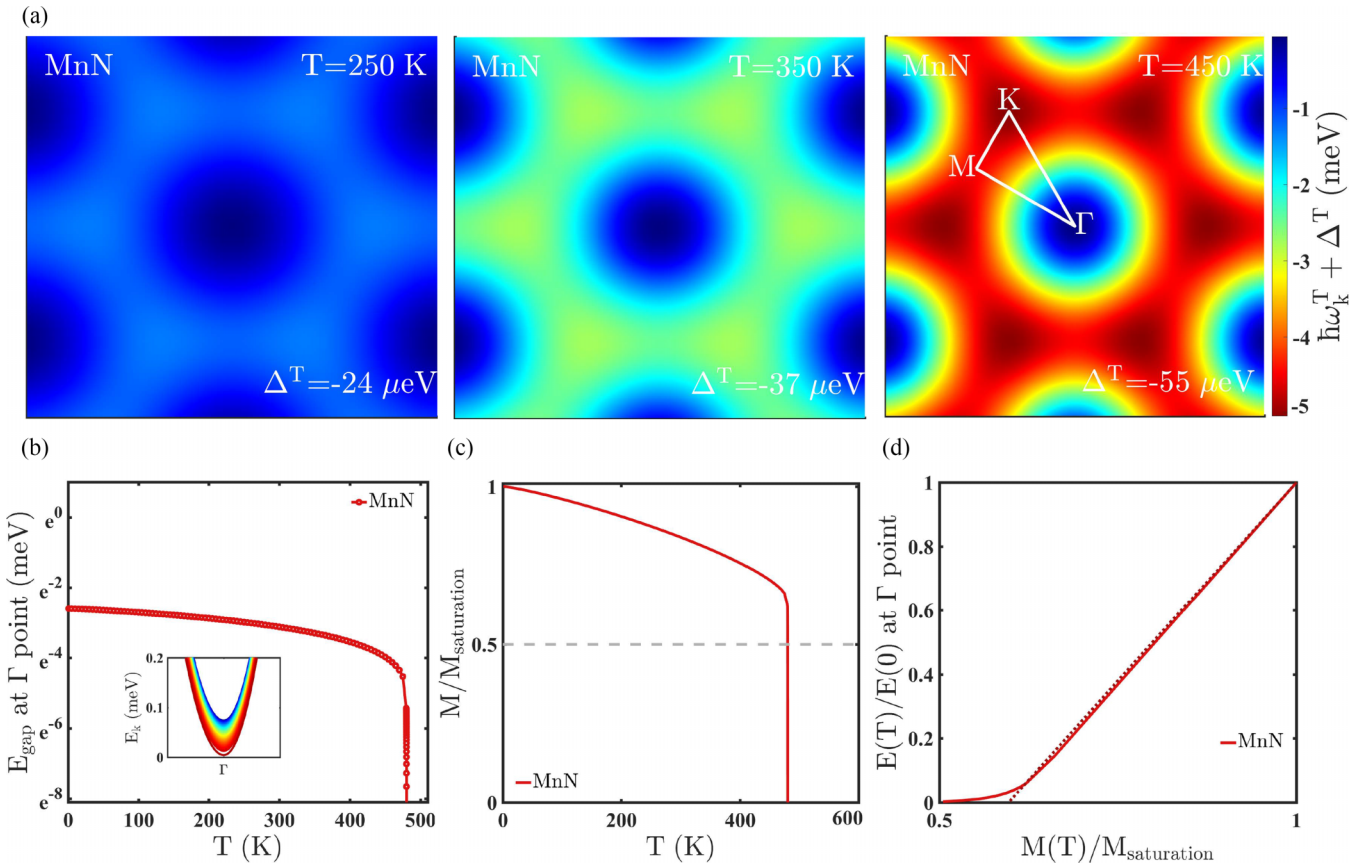

FIG. 4. (a) The $E_{\mathbf{k}}$ in 3D surface as a function of 2D wave vector (k_x, k_y) at different temperatures for MnN monolayer with out-of-plane magnetic anisotropy. The white line displays the high-symmetry path and the sequential color map reflects the magnitude of magnon energy. (b) The curve indicates the temperature dependence of the $E_{\mathbf{k}}$ at the Γ point. The inset shows the $E_{\mathbf{k}}(T)$ around the Γ point. (c) The normalized magnetization as a function of temperature and (d) variation of the magnon energy gap at the Γ point with normalized magnetization in the second-order HP approximation for MnN monolayer.

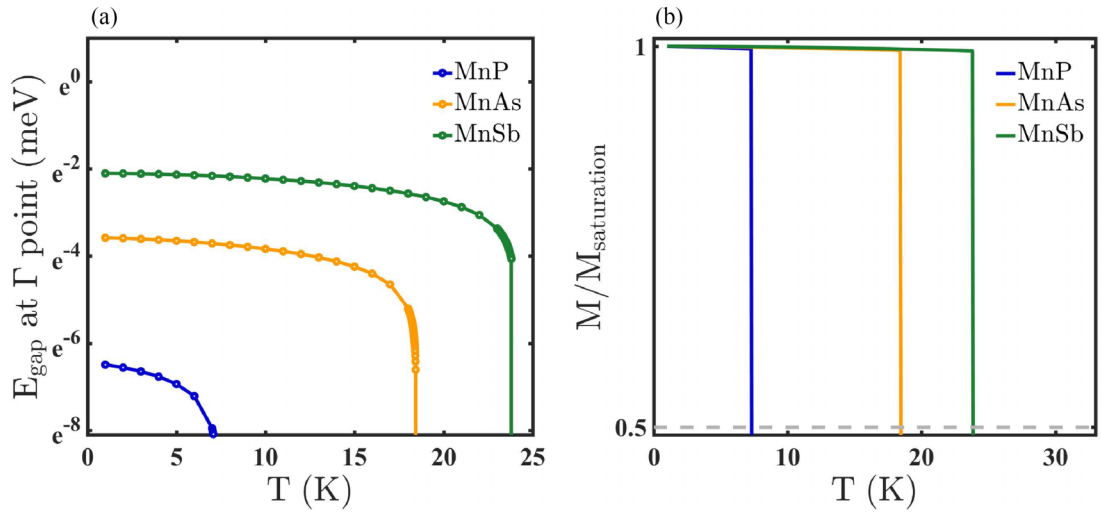

FIG. 5. (a) The temperature dependence of the $E_{\mathbf{k}}$ at the Γ point and (b) $M(T)$ obtained from the second-order HP approximation for MnX (X = P, As, and Sb) monolayers with in-plane magnetic anisotropy.

is dominated by small wave vectors close to the Γ point. At low temperatures, the region where the magnon density and interactions are weak, the magnetization is slowly decreasing. By inclusion of magnon-magnon interaction in the second-order HP approximation, the energy gap is closing at the Γ point [see Figs. 4(b) and 5(a)] and the magnetization drops sharply to zero. The dramatic change in the behavior of magnetization in the second-order HP is related to the resonance between closing the magnon energy gap and the reducing magnetization by the inclusion of magnon-magnon interaction in the second-order HP approximation. For the MnN with out-of-plane easy axis, the magnon energy gap is closed at $T = 480$ K. The estimated Curie temperature in the first-order HP with energy normalization with magnetization [10] is $T_C^1 = 820$ K. As a result according to Fig. 4(b), the Curie temperature is well above the room temperature. Our results are consistent with the previous theoretical estimation of the Curie temperature equal to 368 K for the hexagonal MnN monolayer [67]. For the case of monolayers with an easy axis inside the plane, the magnon energy gap is closed at a very low temperature and the value of Curie temperature tends to zero ($T < 30$ K). The Curie temperatures for in-plane easy-axis monolayers are much lower compared to the first HP approximation (445–585 K), which is due to the magnon energy gap renormalization. The low Curie temperature is related to the negligible Γ parameter and consistent with the Mermin-Wagner-Hohenberg theorem. The Γ parameter makes one of the in-plane axes (x or y) energetically favorable. When the energy of magnons becomes larger than the Γ parameter, the magnetic moments do not have a favorable in-plane axis; instead, they are randomly oriented inside the plane, yielding zero net magnetization at low temperatures. We examine the normalized magnon energy at the Γ point as a function of normalized magnetization for the MnN monolayer in Fig. 4(d). The normalized magnon energy reduces linearly (the dashed line) with magnetization at low temperatures. At higher temperatures, the normalized magnon energy curve deviates from the linear behavior, which is in contrast to the previous approach with simple renormalization of magnon energy [10].

IV. CONCLUSION

In summary, we have studied the electronic and magnetic properties of 2D hexagonal manganese pnictogen monolayers within the density functional theory and second-order Holstein-Primakoff approximation of the anisotropic Heisenberg spin model. The hexagonal MnX monolayers are dynamically and thermally stable with half-metallic electronic structure. The ground state is the ferromagnetic arrangement of Mn moments with an out-of-plane easy axis for MnN and an in-plane easy axis for other monolayers. The effective anisotropic Heisenberg Hamiltonian parameters are obtained from the DFT total energy differences of Mn spin configurations. The magnon energy renormalization is small in the entire first Brillouin zone. However, the reduced magnon excitation energy gap at the Γ point is crucially important for the temperature dependence of magnetization of a 2D magnetic monolayer. By closing the magnon gap, the number of excited magnetic states becomes infinite and magnetization becomes zero. As a result, the Curie temperature is dramatically reduced by the consideration of anharmonic effects (the magnon-magnon interaction). Furthermore, the Curie temperature drop in the structures (MnX, X = P, As, and Sb) having in-plane easy axis is significantly larger than the MnN. This difference is devoted to the trivial value of the Γ parameter, which is responsible for the long-range ferromagnetic order that keeps the magnetic moments along the favorable in-plane axis. Consequently, it is shown that the magnon-magnon coupling has a significant effect on the thermodynamics of magnons and thus the Curie temperature of the structures that renormalize the estimation of first-order HP approximation. We believe that our results provide insight into understanding the many-body effects on the physics of 2D ferromagnetism.

ACKNOWLEDGMENTS

The authors would like to thank A. N. Rudenko and B. S. Kandemir for fruitful discussions. This work was supported by the Scientific and Technological Research

Council of Turkey (TUBITAK) under Project No. 119F361. The numerical calculations reported in this paper were performed at TUBITAK ULAKBIM, High Performance and Grid Computing Center (TRUBA resources).

APPENDIX A: CALCULATION OF ANISOTROPIC HEISENBERG SPIN HAMILTONIAN

The parameters of the anisotropic Heisenberg spin Hamiltonian can be derived from the total energy difference between different magnetic configurations. For the two Hamiltonians for the in-plane and out-of-plane easy axis in the paper, the parameters are derived from the following equations.

1. In-plane easy axis

The effective parameters for monolayers with in-plane easy axis

$$\begin{aligned} J &= \frac{3E_{AFM_z} - 2E_{FM_y} - E_{FM_x}}{24S^2}, \\ A &= \frac{3E_{AFM_x} - 3E_{AFM_z} + E_{FM_x} - E_{FM_z}}{4S^2}, \\ \delta &= \frac{3E_{AFM_z} - 3E_{AFM_x} - 3E_{FM_z} + E_{FM_x} + 2E_{FM_y}}{24S^2}, \\ \Gamma &= \frac{E_{FM_y} - E_{FM_x}}{8S^2}. \end{aligned} \tag{A1}$$

Here the FM and AFM are referring to the ferromagnetic and antiferromagnetic spin configurations, respectively. Also, the indices (x, y, and z) are referring to the spin direction.

2. Out-of-plane easy axis

The effective parameters for monolayers with out-of-plane easy axis

$$\begin{aligned} J &= \frac{E_{AFM_x} - E_{FM_x}}{8S^2}, \\ A &= \frac{3E_{AFM_x} - 3E_{AFM_z} + E_{FM_x} - E_{FM_z}}{4S^2}, \\ \delta &= \frac{E_{AFM_z} - E_{AFM_x} - E_{FM_z} + E_{FM_x}}{8S^2}. \end{aligned} \tag{A2}$$

APPENDIX B: DERIVATION OF THE MAGNON DISPERSION RELATION INCLUDING MAGNON INTERACTIONS

1. In-plane easy-axis spin Hamiltonian

We consider H assuming the preferred spin direction along the x axis, Eq. (1), represented as

$$\begin{aligned} H &= H_1 + H_2 + H_3 + H_4, \\ H_1 &= -\frac{J}{2}\sum_{\langle ij\rangle} \mathbf{S}_i \cdot \mathbf{S}_j, \quad H_2 = -\frac{\Gamma}{2}\sum_{\langle ij\rangle}\left(S_i^x S_j^y + S_i^y S_j^x\right), \\ H_3 &= -\frac{\delta}{2}\sum_{\langle ij\rangle} S_i^z S_j^z, \quad H_4 = -A\sum_i \left(S_i^z\right)^2. \end{aligned} \tag{B1}$$

Next, we consider each term of H separately. We consider the isotropic pairwise nearest-neighbor interactions satisfying $J_{\langle ij\rangle} = J$, which results in $J_{\mathbf{k}} = J_{-\mathbf{k}}$ symmetry. Furthermore, we have $\delta_{\langle ij\rangle} = \delta$, $\Gamma_{\langle ij\rangle} = \Gamma$, and $A_i = A$.

The H_1 can be rewritten using the spin ladder operators as

$$H_1 = -\frac{J}{2}\sum_{\langle ij\rangle}\left(\frac{1}{2}(S_i^+ S_j^- + S_i^- S_j^+) + S_i^x S_j^x\right).$$

Regarding the second-order approximation of HP transformations, $S_i^- \approx \sqrt{2S}(a_i - \frac{a_i^\dagger a_i a_i}{4S})$ and $S_i^+ \approx \sqrt{2S}(a_i^\dagger - \frac{a_i^\dagger a_i^\dagger a_i}{4S})$, the total Hamiltonian is $H = H^0 + H^T$; H^0 is a bilinear form of the magnon operators, while the H^T concerns the magnon-magnon two-particle interactions. Therefore,

$$H_1^0 = -\frac{J}{2}S\sum_{\langle ij\rangle}(a_j^\dagger a_i + a_i^\dagger a_j - 2a_i^\dagger a_i)$$

and

$$\begin{aligned} H_1^T = -\frac{J}{2}\sum_{\langle ij\rangle}\Bigg(\frac{-1}{4}(&a_i^\dagger a_j^\dagger a_j a_j + a_i^\dagger a_i^\dagger a_i a_j \\ &+ a_j^\dagger a_i^\dagger a_i a_i + a_j^\dagger a_j^\dagger a_j a_i) + (a_i^\dagger a_j^\dagger a_i a_j)\Bigg). \end{aligned}$$

We now transform the real-space creation and annihilation operators to the reciprocal space with the help of the Fourier transforms,

$$a_i^\dagger = \frac{1}{\sqrt{N}}\sum_{\mathbf{k}} e^{-i\mathbf{k}\cdot\mathbf{R}_i} a_{\mathbf{k}}^\dagger, \quad a_i = \frac{1}{\sqrt{N}}\sum_{\mathbf{k}} e^{i\mathbf{k}\cdot\mathbf{R}_i} a_{\mathbf{k}}.$$

Here N represents the number of sites. Considering $\sum_{\langle ij\rangle} = \sum_{\mathbf{R}_i}\sum_{\Delta\mathbf{R}}$, $\Delta\mathbf{R} = \mathbf{R}_i - \mathbf{R}_j$ and $\frac{1}{N}\sum_{\mathbf{R}_i} e^{-i(\mathbf{k}-\mathbf{k}')\cdot\mathbf{R}_i} = \delta_{\mathbf{k}\mathbf{k}'}$, one obtains H_1 given by

$$H_1^0 = \sum_{\mathbf{k}}\left(SJ\sum_{\Delta\mathbf{R}}(1 - \cos\mathbf{k}\cdot\Delta\mathbf{R})\right)a_{\mathbf{k}}^\dagger a_{\mathbf{k}}$$

and

$$\begin{aligned} H_1^T = -\frac{J}{2N}\sum_{\mathbf{k}\mathbf{k}'\mathbf{k}''}\sum_{\Delta\mathbf{R}} a_{\mathbf{k}}^\dagger a_{\mathbf{k}'}^\dagger a_{\mathbf{k}''} a_{\mathbf{k}+\mathbf{k}'-\mathbf{k}''}[e^{i(\mathbf{k}-\mathbf{k}'')\cdot\Delta\mathbf{R}} \\ - \frac{1}{2}(\cos((\mathbf{k}+\mathbf{k}'-\mathbf{k}'')\cdot\Delta\mathbf{R}) + \cos(\mathbf{k}\cdot\Delta\mathbf{R}))]. \end{aligned}$$

Generating a rotation through 45° about the z axis, in the rotated frame, H_2 takes the form

$$\begin{aligned} H_2 &= -\frac{\Gamma}{2}\sum_{\langle ij\rangle}\left(S_i^x S_j^x - S_i^y S_j^y\right) = H_2(1) + H_2(2), \\ H_2(1) &= -\frac{\Gamma}{2}\sum_{\langle ij\rangle} S_i^x S_j^x, \quad H_2(2) = \frac{\Gamma}{2}\sum_{\langle ij\rangle} S_i^y S_j^y. \end{aligned} \tag{B2}$$

The second-order HP transformation yields

$$H_2^0(1) = \Gamma S \sum_{\langle ij \rangle} a_i^\dagger a_i,$$

$$H_2^0(2) = -\frac{\Gamma S}{4} \sum_{\langle ij \rangle} (a_i^\dagger a_j^\dagger - 2a_i^\dagger a_j + a_i a_j),$$

$$H_2^T(1) = -\frac{\Gamma}{2} \sum_{\langle ij \rangle} a_i^\dagger a_j^\dagger a_i a_j,$$

$$H_2^T(2) = \frac{\Gamma}{8} \sum_{\langle ij \rangle} (a_j^\dagger a_i^\dagger a_i^\dagger a_i - a_i^\dagger a_i^\dagger a_i a_j - a_j^\dagger a_i^\dagger a_i a_i + a_i^\dagger a_i a_i a_j).$$

After the Fourier transformation, we obtain

$$H_2^0(1) = \Gamma S Z \sum_{\mathbf{k}} a_{\mathbf{k}}^\dagger a_{\mathbf{k}},$$

$$H_2^0(2) = \frac{-\Gamma S}{4} \sum_{\mathbf{k}} \sum_{\mathbf{\Delta R}} e^{i\mathbf{k}\cdot\mathbf{\Delta R}} (a_{\mathbf{k}}^\dagger a_{-\mathbf{k}}^\dagger - 2a_{\mathbf{k}}^\dagger a_{\mathbf{k}} + a_{\mathbf{k}} a_{-\mathbf{k}}),$$

$$H_2^T(1) = -\frac{\Gamma}{2N} \sum_{\mathbf{k}\mathbf{k}'\mathbf{k}''} \sum_{\mathbf{\Delta R}} (e^{i(\mathbf{k}-\mathbf{k}'')\cdot\mathbf{\Delta R}}) a_{\mathbf{k}}^\dagger a_{\mathbf{k}'}^\dagger a_{\mathbf{k}''} a_{\mathbf{k}+\mathbf{k}'-\mathbf{k}''},$$

$$H_2^T(2) = \frac{\Gamma}{8N} \sum_{\mathbf{k}\mathbf{k}'\mathbf{k}''} \sum_{\mathbf{\Delta R}} [(-e^{i(\mathbf{k}+\mathbf{k}'-\mathbf{k}'')\cdot\mathbf{\Delta R}} - e^{-i\mathbf{k}\cdot\mathbf{\Delta R}}) a_{\mathbf{k}}^\dagger a_{\mathbf{k}'}^\dagger a_{\mathbf{k}''} a_{\mathbf{k}+\mathbf{k}'-\mathbf{k}''} + (e^{-i\mathbf{k}\cdot\mathbf{\Delta R}}) a_{\mathbf{k}}^\dagger a_{\mathbf{k}'}^\dagger a_{\mathbf{k}''}^\dagger a_{\mathbf{k}+\mathbf{k}'+\mathbf{k}''}$$
$$+ (e^{i(\mathbf{k}-\mathbf{k}'-\mathbf{k}'')\cdot\mathbf{\Delta R}}) a_{\mathbf{k}}^\dagger a_{\mathbf{k}'} a_{\mathbf{k}''} a_{\mathbf{k}-\mathbf{k}'-\mathbf{k}''}].$$

Here, Z is the number of nearest neighbors. The third term in the Hamiltonian, H_3, leads in the same way to

$$H_3^0 = \frac{-\delta S}{4} \sum_{\langle ij \rangle} (a_i^\dagger a_j^\dagger + 2a_i^\dagger a_j + a_i a_j),$$

$$H_3^T = \frac{\delta}{8} \sum_{\langle ij \rangle} (a_j^\dagger a_i^\dagger a_i^\dagger a_i + a_i^\dagger a_i^\dagger a_i a_j + a_j^\dagger a_i^\dagger a_i a_i + a_i^\dagger a_i a_i a_j).$$

The Fourier representation yields

$$H_3^0 = -\frac{\delta S}{4} \sum_{\mathbf{k}} \sum_{\mathbf{\Delta R}} e^{i\mathbf{k}\cdot\mathbf{\Delta R}} (a_{\mathbf{k}}^\dagger a_{-\mathbf{k}}^\dagger + 2a_{\mathbf{k}}^\dagger a_{\mathbf{k}} + a_{\mathbf{k}} a_{-\mathbf{k}}),$$

$$H_3^T = \frac{\delta}{8N} \sum_{\mathbf{k}\mathbf{k}'\mathbf{k}''} \sum_{\mathbf{\Delta R}} [(e^{i(\mathbf{k}+\mathbf{k}'-\mathbf{k}'')\cdot\mathbf{\Delta R}} + e^{-i\mathbf{k}\cdot\mathbf{\Delta R}}) a_{\mathbf{k}}^\dagger a_{\mathbf{k}'}^\dagger a_{\mathbf{k}''} a_{\mathbf{k}+\mathbf{k}'-\mathbf{k}''} + (e^{-i\mathbf{k}\cdot\mathbf{\Delta R}}) a_{\mathbf{k}}^\dagger a_{\mathbf{k}'}^\dagger a_{\mathbf{k}''}^\dagger a_{\mathbf{k}+\mathbf{k}'+\mathbf{k}''}$$
$$+ (e^{i(\mathbf{k}-\mathbf{k}'-\mathbf{k}'')\cdot\mathbf{\Delta R}}) a_{\mathbf{k}}^\dagger a_{\mathbf{k}'} a_{\mathbf{k}''} a_{\mathbf{k}-\mathbf{k}'-\mathbf{k}''}].$$

By using the second-order approximation of HP followed by the Fourier transformation for H_4,

$$H_4^0 = \sum_i \frac{-AS}{2} (a_i^\dagger a_i^\dagger + 2a_i^\dagger a_i + a_i a_i),$$

$$H_4^T = \frac{A}{4} \sum_i (a_i^\dagger a_i^\dagger a_i^\dagger a_i + 2a_i^\dagger a_i^\dagger a_i a_i + a_i^\dagger a_i a_i a_i),$$

and

$$H_4^0 = \sum_{\mathbf{k}} -\frac{AS}{2} (a_{\mathbf{k}}^\dagger a_{-\mathbf{k}}^\dagger + 2a_{\mathbf{k}}^\dagger a_{\mathbf{k}} + a_{\mathbf{k}} a_{-\mathbf{k}}),$$

$$H_4^T = \frac{A}{4N} \sum_{\mathbf{k}\mathbf{k}'\mathbf{k}''} (2a_{\mathbf{k}}^\dagger a_{\mathbf{k}'}^\dagger a_{\mathbf{k}''} a_{\mathbf{k}+\mathbf{k}'-\mathbf{k}''} + a_{\mathbf{k}}^\dagger a_{\mathbf{k}'}^\dagger a_{\mathbf{k}''}^\dagger a_{\mathbf{k}+\mathbf{k}'+\mathbf{k}''} + a_{\mathbf{k}}^\dagger a_{\mathbf{k}'} a_{\mathbf{k}''} a_{\mathbf{k}-\mathbf{k}'-\mathbf{k}''}).$$

By combining all parts of Hamiltonian, the final interacting magnons Hamiltonian can be written as

$$H_{\text{total}} = +\sum_{\mathbf{k}} a_{\mathbf{k}}^{\dagger} a_{\mathbf{k}} \left(\left(J + \Gamma - \frac{A}{Z} \right) SZ + S\left(-J + \frac{\Gamma}{2} - \frac{\delta}{2} \right) f(\mathbf{k}) \right) + \sum_{\mathbf{k}} a_{\mathbf{k}}^{\dagger} a_{-\mathbf{k}}^{\dagger} \left(-\frac{A}{2} S - \frac{S}{4}(\Gamma + \delta) f(\mathbf{k}) \right)$$
$$+ \sum_{\mathbf{k}} a_{\mathbf{k}} a_{-\mathbf{k}} \left(-\frac{A}{2} S - \frac{S}{4}(\Gamma + \delta) f(\mathbf{k}) \right) + \sum_{\mathbf{k}\mathbf{k}'\mathbf{k}''} \left[a_{\mathbf{k}}^{\dagger} a_{\mathbf{k}'}^{\dagger} a_{\mathbf{k}''} a_{\mathbf{k}+\mathbf{k}'-\mathbf{k}''} \left(\frac{A}{2N} + \sum_{\Delta\mathbf{R}} \left[-\frac{J+\Gamma}{2N} f(\mathbf{k}-\mathbf{k}'') \right. \right. \right.$$
$$\left. + \frac{2J - \Gamma + \delta}{8N} (f(\mathbf{k}+\mathbf{k}'-\mathbf{k}'') + f(\mathbf{k})) \right] \Bigg) + a_{\mathbf{k}}^{\dagger} a_{\mathbf{k}'}^{\dagger} a_{\mathbf{k}''}^{\dagger} a_{\mathbf{k}+\mathbf{k}'+\mathbf{k}''} \left(\frac{A}{4N} + \sum_{\Delta\mathbf{R}} \left(\frac{\Gamma + \delta}{8N} f(\mathbf{k}) \right) \right)$$
$$\left. + a_{\mathbf{k}}^{\dagger} a_{\mathbf{k}'} a_{\mathbf{k}''} a_{\mathbf{k}-\mathbf{k}'-\mathbf{k}''} \left(\frac{A}{4N} + \sum_{\Delta\mathbf{R}} \left(\frac{\Gamma + \delta}{8N} f(\mathbf{k}-\mathbf{k}'-\mathbf{k}'') \right) \right) \right], \tag{B3}$$

where for hexagonal lattice,

$$f(\mathbf{k}) = \sum_{\Delta\mathbf{R}} e^{-i\mathbf{k}\cdot\Delta\mathbf{R}}$$
$$= 2\left[\cos k_x a + 2\cos\left(\frac{1}{2} k_x a \right) \cos\left(\frac{\sqrt{3}}{2} k_y a \right) \right].$$

Since no analytical solution is possible, a Hartree-Fock decoupling is applied to the fourfold interactive Hamiltonian [41,80],

$$a_{\mathbf{k}}^{\dagger} a_{\mathbf{k}'}^{\dagger} a_{\mathbf{k}''} a_{\mathbf{k}+\mathbf{k}'-\mathbf{k}''} \cong \langle a_{\mathbf{k}}^{\dagger} a_{\mathbf{k}+\mathbf{k}'-\mathbf{k}''} \rangle a_{\mathbf{k}'}^{\dagger} a_{\mathbf{k}''} + \langle a_{\mathbf{k}'}^{\dagger} a_{\mathbf{k}''} \rangle a_{\mathbf{k}}^{\dagger} a_{\mathbf{k}+\mathbf{k}'-\mathbf{k}''}$$
$$+ \langle a_{\mathbf{k}}^{\dagger} a_{\mathbf{k}''} \rangle a_{\mathbf{k}'}^{\dagger} a_{\mathbf{k}+\mathbf{k}'-\mathbf{k}''} + \langle a_{\mathbf{k}'}^{\dagger} a_{\mathbf{k}+\mathbf{k}'-\mathbf{k}''} \rangle$$
$$\times\ a_{\mathbf{k}}^{\dagger} a_{\mathbf{k}''},$$
$$a_{\mathbf{k}}^{\dagger} a_{\mathbf{k}'}^{\dagger} a_{\mathbf{k}''}^{\dagger} a_{\mathbf{k}+\mathbf{k}'+\mathbf{k}''} \cong \langle a_{\mathbf{k}}^{\dagger} a_{\mathbf{k}+\mathbf{k}'+\mathbf{k}''} \rangle a_{\mathbf{k}'}^{\dagger} a_{\mathbf{k}''}^{\dagger} + \langle a_{\mathbf{k}'}^{\dagger} a_{\mathbf{k}+\mathbf{k}'+\mathbf{k}''} \rangle a_{\mathbf{k}}^{\dagger} a_{\mathbf{k}''}^{\dagger}$$
$$+ \langle a_{\mathbf{k}''}^{\dagger} a_{\mathbf{k}+\mathbf{k}'+\mathbf{k}''} \rangle a_{\mathbf{k}}^{\dagger} a_{\mathbf{k}'}^{\dagger}$$

and

$$a_{\mathbf{k}}^{\dagger} a_{\mathbf{k}'} a_{\mathbf{k}''} a_{\mathbf{k}-\mathbf{k}'-\mathbf{k}''} \cong \langle a_{\mathbf{k}}^{\dagger} a_{\mathbf{k}'} \rangle a_{\mathbf{k}''} a_{\mathbf{k}-\mathbf{k}'-\mathbf{k}''} + \langle a_{\mathbf{k}}^{\dagger} a_{\mathbf{k}''} \rangle a_{\mathbf{k}'} a_{\mathbf{k}-\mathbf{k}'-\mathbf{k}''}$$
$$+ \langle a_{\mathbf{k}}^{\dagger} a_{\mathbf{k}-\mathbf{k}'-\mathbf{k}''} \rangle a_{\mathbf{k}'}^{\dagger} a_{\mathbf{k}''}.$$

By considering $\langle a_{\mathbf{k}}^{\dagger} a_{\mathbf{k}'} \rangle = \delta_{\mathbf{k},\mathbf{k}'} n_{\mathbf{k}}$, the interactive magnon Hamiltonian can be written as

$$H_{\text{total}} = \sum_{\mathbf{k}} \beta_{\mathbf{k}} a_{\mathbf{k}}^{\dagger} a_{\mathbf{k}} + \sum_{\mathbf{k}} \alpha_{\mathbf{k}} a_{\mathbf{k}}^{\dagger} a_{-\mathbf{k}}^{\dagger} + \sum_{\mathbf{k}} \alpha_{\mathbf{k}} a_{\mathbf{k}} a_{-\mathbf{k}}, \tag{B4}$$

while $\beta_{\mathbf{k}} = \hbar\omega_{\mathbf{k}}^{0} + \hbar\omega_{\mathbf{k}}^{T} + \Delta^{0} + \Delta^{T}$,

$$\hbar\omega_{\mathbf{k}} = \hbar\omega_{\mathbf{k}}^{0} + \hbar\omega_{\mathbf{k}}^{T}$$
$$= \sum_{\Delta\mathbf{R}} S\left(\frac{2J - \Gamma + \delta}{2} \right) \left(1 - \cos(\mathbf{k}\cdot\Delta\mathbf{R}) \right)$$
$$\times \left(1 - \frac{1}{NS} \sum_{\mathbf{k}'} n_{\mathbf{k}'} \left(1 - \frac{2(J+\Gamma)}{2J - \Gamma + \delta} \cos(\mathbf{k}'\cdot\Delta\mathbf{R}) \right) \right), \tag{B5}$$

$$\Delta = \Delta^{0} + \Delta^{T}$$
$$= \left((3\Gamma - \delta)\frac{SZ}{2} - AS \right) - \sum_{\mathbf{k}'} n_{\mathbf{k}'} \left(\frac{(3\Gamma - \delta)Z - 4A}{2N} \right.$$
$$\left. + \frac{3\Gamma - \delta}{2N} \sum_{\Delta\mathbf{R}} \cos(\mathbf{k}'\cdot\Delta\mathbf{R}) \right) \tag{B6}$$

and

$$\alpha_{\mathbf{k}} = \alpha_{\mathbf{k}}^{0} + \alpha_{\mathbf{k}}^{T}$$
$$= \left(-\frac{A}{2} S - \frac{S}{4}(\Gamma + \delta) \sum_{\Delta\mathbf{R}} \cos(\mathbf{k}\cdot\Delta\mathbf{R}) \right)$$
$$+ \left(\sum_{\mathbf{k}'} n_{\mathbf{k}'} \left[3\frac{A}{4N} + \frac{\Gamma + \delta}{8N} \left(2\sum_{\Delta\mathbf{R}} \cos(\mathbf{k}\cdot\Delta\mathbf{R}) \right. \right. \right.$$
$$\left. \left. \left. + \sum_{\Delta\mathbf{R}} \cos(\mathbf{k}'\cdot\Delta\mathbf{R}) \right) \right] \right). \tag{B7}$$

We apply a unitary transformation to remove the nondiagonal terms ($\alpha_{\mathbf{k}} \neq 0$) and calculate the interactive magnon energy [38],

$$E_{\mathbf{k}} = \sqrt{(\beta_{\mathbf{k}})^2 - 4(\alpha_{\mathbf{k}})^2}. \tag{B8}$$

2. Out-of-plane easy-axis spin Hamiltonian

Regarding $S^{\pm} = S^{x} \pm iS^{y}$, the anisotropic Heisenberg Hamiltonian, Eq. (8), can be written as

$$H = -\frac{J}{2} \sum_{\langle ij \rangle} \left(\frac{1}{2}(S_i^{+} S_j^{-} + S_i^{-} S_j^{+}) + S_i^{z} S_j^{z} \right)$$
$$- \frac{\delta}{2} \sum_{\langle ij \rangle} S_i^{z} S_j^{z} - A \sum_{i} \left(S_i^{z} \right)^2. \tag{B9}$$

Based on the second-order HP approximation denoting that $S_i^{+} \approx \sqrt{2S}(a_i - \frac{a_i^{\dagger} a_i a_i}{4S})$ and $S_i^{-} \approx \sqrt{2S}(a_i^{\dagger} - \frac{a_i^{\dagger} a_i^{\dagger} a_i}{4S})$, H^{0} and

H^T are given by

$$H^0 = -\frac{JS}{2}\sum_{\langle ij\rangle}(a_j^\dagger a_i + a_i^\dagger a_j - 2a_i^\dagger a_i) + [A(2S-1) + S\delta Z]\sum_i a_i^\dagger a_i, \tag{B10}$$

$$H^T = -\frac{J}{2}\sum_{\langle ij\rangle}\Big[a_i^\dagger a_j^\dagger a_i a_j - \frac{1}{4}(a_j^\dagger a_j^\dagger a_j a_i + a_j^\dagger a_i^\dagger a_i a_i + a_i^\dagger a_j^\dagger a_j a_j + a_i^\dagger a_i^\dagger a_i a_j)\Big] - \frac{\delta}{2}\sum_{\langle ij\rangle}(a_i^\dagger a_j^\dagger a_i a_j) - A\sum_i (a_i^\dagger a_i^\dagger a_i a_i). \tag{B11}$$

Applying the Fourier transformation and performing calculations like the previous section of this Appendix,

$$E_{\mathbf{k}} = \hbar\omega_{\mathbf{k}}^0 + \hbar\omega_{\mathbf{k}}^T + \Delta^0 + \Delta^T, \tag{B12}$$

where

$$\hbar\omega_{\mathbf{k}} = \hbar\omega_{\mathbf{k}}^T + \hbar\omega_{\mathbf{k}}^0 = SJ\sum_{\Delta\mathbf{R}}(1-\cos(\mathbf{k}\cdot\Delta\mathbf{R})) \times\left[1 - \frac{1}{NS}\sum_{\mathbf{k}'}\left(1 - \frac{(J+\delta)}{J}\cos(\mathbf{k}'\cdot\Delta\mathbf{R})\right)n_{\mathbf{k}'}\right] \tag{B13}$$

and

$$\Delta = \Delta^0 + \Delta^T = [A(2S-1) + S\delta Z] - \frac{\delta}{N}\sum_{\Delta\mathbf{R}}\sum_{\mathbf{k}'}(\cos(\mathbf{k}'\cdot\Delta R))n_{\mathbf{k}'} - \frac{(\delta + 4A/Z)}{N}\sum_{\Delta\mathbf{R}}\sum_{\mathbf{k}'}n_{\mathbf{k}'}. \tag{B14}$$

[1] B. Huang, G. Clark, E. Navarro-Moratalla, D. R. Klein, R. Cheng, K. L. Seyler, D. Zhong, E. Schmidgall, M. A. McGuire, D. H. Cobden, W. Yao, D. Xiao, P. Jarillo-Herrero, and X. Xu, Layer-dependent ferromagnetism in a van der Waals crystal down to the monolayer limit, Nature (London) **546**, 270 (2017).

[2] K. S. Burch, D. Mandrus, and J.-G. Park, Magnetism in two-dimensional van der Waals materials, Nature (London) **563**, 47 (2018).

[3] K. F. Mak, J. Shan, and D. C. Ralph, Probing and controlling magnetic states in 2D layered magnetic materials, Nat. Rev. Phys. **1**, 646 (2019).

[4] M. Gibertini, M. Koperski, A. F. Morpurgo, and K. S. Novoselov, Magnetic 2D materials and heterostructures, Nat. Nanotechnol. **14**, 408 (2019).

[5] X.-X. Zhang, L. Li, D. Weber, J. Goldberger, K. F. Mak, and J. Shan, Gate-tunable spin waves in antiferromagnetic atomic bilayers, Nat. Mater. **19**, 838 (2020).

[6] C. Ataca, H. Sahin, and S. Ciraci, Stable, single-layer MX_2 transition-metal oxides and dichalcogenides in a honeycomb-like structure, J. Phys. Chem. C **116**, 8983 (2012).

[7] T. Song, Z. Fei, M. Yankowitz, Z. Lin, Q. Jiang, K. Hwangbo, Q. Zhang, B. Sun, T. Taniguchi, K. Watanabe, M. A. McGuire, D. Graf, T. Cao, J.-H. Chu, D. H. Cobden, C. R. Dean, D. Xiao, and X. Xu, Switching 2D magnetic states via pressure tuning of layer stacking, Nat. Mater. **18**, 1298 (2019).

[8] A. Mogulkoc, M. Modarresi, and A. N. Rudenko, Two-dimensional chromium pnictides $CrX(X = \mathrm{P}, \mathrm{As}, \mathrm{Sb})$: Half-metallic ferromagnets with high Curie temperature, Phys. Rev. B **102**, 024441 (2020).

[9] M. Modarresi, A. Mogulkoc, Y. Mogulkoc, and A. N. Rudenko, Erratum: Lateral Spin Valve Based on the Two-Dimensional CrN/P/CrN heterostructure [Phys. Rev. Appl. **11**, 064015 (2019)], Phys. Rev. Appl. **13**, 069901(E) (2020).

[10] J. L. Lado and J. Fernández-Rossier, On the origin of magnetic anisotropy in two dimensional CrI_3, 2D Mater. **4**, 035002 (2017).

[11] M. Bonilla, S. Kolekar, Y. Ma, H. C. Diaz, V. Kalappattil, R. Das, T. Eggers, H. R. Gutierrez, M.-H. Phan, and M. Batzill, Strong room-temperature ferromagnetism in VSe_2 monolayers on van der Waals substrates, Nat. Nanotechnol. **13**, 289 (2018).

[12] Y. Guo, S. Zhou, and J. Zhao, Two-dimensional intrinsic ferromagnets with high Curie temperatures: Synthesis, physical properties and device applications, J. Mater. Chem. C **9**, 6103 (2021).

[13] Y. Deng, Y. Yu, Y. Song, J. Zhang, N. Z. Wang, Z. Sun, Y. Yi, Y. Z. Wu, S. Wu, J. Zhu, J. Wang, X. H. Chen, and Y. Zhang, Gate-tunable room-temperature ferromagnetism in two-dimensional Fe_3GeTe_2, Nature (London) **563**, 94 (2018).

[14] X. Lu, R. Fei, and L. Yang, Curie temperature of emerging two-dimensional magnetic structures, Phys. Rev. B **100**, 205409 (2019).

[15] H. H. Kim, B. Yang, S. Li, S. Jiang, C. Jin, Z. Tao, G. Nichols, F. Sfigakis, S. Zhong, C. Li, S. Tian, D. G. Cory, G.-X. Miao, J. Shan, K. F. Mak, H. Lei, K. Sun, L. Zhao, and A. W. Tsen, Evolution of interlayer and intralayer magnetism in three atomically thin chromium trihalides, Proc. Natl. Acad. Sci. USA **116**, 11131 (2019).

[16] X. Cai, T. Song, N. P. Wilson, G. Clark, M. He, X. Zhang, T. Taniguchi, K. Watanabe, W. Yao, D. Xiao, M. A. McGuire, D. H. Cobden, and X. Xu, Atomically thin $CrCl_3$: An in-plane layered antiferromagnetic insulator, Nano Lett. **19**, 3993 (2019).

[17] C. Gong, L. Li, Z. Li, H. Ji, A. Stern, Y. Xia, T. Cao, W. Bao, C. Wang, Y. Wang, Z. Q. Qiu, R. J. Cava, S. G. Louie, J. Xia, and X. Zhang, Discovery of intrinsic ferromagnetism in two-dimensional van der Waals crystals, Nature (London) **546**, 265 (2017).

[18] X. Sun, S. Zhao, A. Bachmatiuk, M. H. Rümmeli, S. Gorantla, M. Zeng, and L. Fu, 2D intrinsic ferromagnetic MnP single crystals, Small **16**, 2001484 (2020).

[19] X. Zhang, Q. Lu, W. Liu, W. Niu, J. Sun, J. Cook, M. Vaninger, P. F. Miceli, D. J. Singh, S.-W. Lian, T.-R. Chang, X. He, J. Du, L. He, R. Zhang, G. Bian, and Y. Xu, Room-temperature intrinsic ferromagnetism in epitaxial $CrTe_2$ ultrathin films, Nat. Commun. **12**, 2492 (2021).

[20] S. Zhang, Y. Li, T. Zhao, and Q. Wang, Robust ferromagnetism in monolayer chromium nitride, Sci. Rep. **4**, 5241 (2014).

[21] Q. Sun and N. Kioussis, Prediction of manganese trihalides as two-dimensional Dirac half-metals, Phys. Rev. B **97**, 094408 (2018).

[22] Y. Yue, Fe_2C monolayer: An intrinsic ferromagnetic MXene, J. Magn. Magn. Mater. **434**, 164 (2017).

[23] Y. Zhang, J. Pang, M. Zhang, X. Gu, and L. Huang, Two-dimensional Co_2S_2 monolayer with robust ferromagnetism, Sci. Rep. **7**, 15993 (2017).

[24] Y. Sun, Z. Zhuo, X. Wu, and J. Yang, Room-temperature ferromagnetism in two-dimensional Fe_2Si nanosheet with enhanced spin-polarization ratio, Nano Lett. **17**, 2771 (2017).

[25] J. He, P. Lyu, and P. Nachtigall, New two-dimensional Mn-based MXenes with room-temperature ferromagnetism and half-metallicity, J. Mater. Chem. C **4**, 11143 (2016).

[26] H. Kumar, N. C. Frey, L. Dong, B. Anasori, Y. Gogotsi, and V. B. Shenoy, Tunable magnetism and transport properties in nitride MXenes, ACS Nano **11**, 7648 (2017).

[27] J. He, X. Li, P. Lyu, and P. Nachtigall, Near-room-temperature Chern insulator and Dirac spin-gapless semiconductor: Nickel chloride monolayer, Nanoscale **9**, 2246 (2017).

[28] W. Yu, J. Li, T. S. Herng, Z. Wang, X. Zhao, X. Chi, W. Fu, I. Abdelwahab, J. Zhou, J. Dan *et al.*, Chemically exfoliated VSe_2 monolayers with room-temperature ferromagnetism, Adv. Mater. **31**, 1903779 (2019).

[29] J. Li, B. Zhao, P. Chen, R. Wu, B. Li, Q. Xia, G. Guo, J. Luo, K. Zang, Z. Zhang, H. Ma, G. Sun, X. Duan, and X. Duan, Synthesis of ultrathin metallic MTe_2 (M = V, Nb, Ta) single-crystalline nanoplates, Adv. Mater. **30**, 1801043 (2018).

[30] D. J. O'Hara, T. Zhu, A. H. Trout, A. S. Ahmed, Y. K. Luo, C. H. Lee, M. R. Brenner, S. Rajan, J. A. Gupta, D. W. McComb, and R. K. Kawakami, Room temperature intrinsic ferromagnetism in epitaxial manganese selenide films in the monolayer limit, Nano Lett. **18**, 3125 (2018).

[31] Y. Guo, H. Deng, X. Sun, X. Li, J. Zhao, J. Wu, W. Chu, S. Zhang, H. Pan, X. Zheng, X. Wu, C. Jin, C. Wu, and Y. Xie, Modulation of metal and insulator states in 2D ferromagnetic VS_2 by van der Waals interaction engineering, Adv. Mater. **29**, 1700715 (2017).

[32] N. D. Mermin and H. Wagner, Absence of Ferromagnetism or Antiferromagnetism in One- or Two-Dimensional Isotropic Heisenberg Models, Phys. Rev. Lett. **17**, 1133 (1966).

[33] P. C. Hohenberg, Existence of long-range order in one and two dimensions, Phys. Rev. **158**, 383 (1967).

[34] J. Rusz, I. Turek, and M. Diviš, Random-phase approximation for critical temperatures of collinear magnets with multiple sublattices: GdX compounds (X = Mg, Rh, Ni, Pd), Phys. Rev. B **71**, 174408 (2005).

[35] L. Liu, I. Kankam, and H. L. Zhuang, Single-layer antiferromagnetic semiconductor CoS_2 with pentagonal structure, Phys. Rev. B **98**, 205425 (2018).

[36] V. V. Kulish and W. Huang, Single-layer metal halides MX_2 (X = Cl, Br, I): Stability and tunable magnetism from first principles and Monte Carlo simulations, J. Mater. Chem. C **5**, 8734 (2017).

[37] Z. Jiang, P. Wang, X. Jiang, and J. Zhao, MBene (MnB): A new type of 2D metallic ferromagnet with high Curie temperature, Nanoscale Horiz. **3**, 335 (2018).

[38] S. Memarzadeh, M. R. Roknabadi, M. Modarresi, A. Mogulkoc, and A. N. Rudenko, Role of charge doping and strain in the stabilization of in-plane ferromagnetism in monolayer VSe_2 at room temperature, 2D Mater. **8**, 035022 (2021).

[39] M. Azmoonfar, M. Roknabadi, M. Modarresi, and A. Mogulkoc, Characterization of two dimensional ferromagnetic binary and Janus manganese dichalcogenides, J. Magn. Magn. Mater. **556**, 169412 (2022).

[40] F. Bloch, Zur theorie des ferromagnetismus, Z. Phys. **61**, 206 (1930).

[41] Z. Li, T. Cao, and S. G. Louie, Two-dimensional ferromagnetism in few-layer van der Waals crystals: Renormalized spin-wave theory and calculations, J. Magn. Magn. Mater. **463**, 28 (2018).

[42] B. Wei, J.-J. Zhu, Y. Song, and K. Chang, Renormalization of gapped magnon excitation in monolayer $MnBi_2Te_4$ by magnon-magnon interaction, Phys. Rev. B **104**, 174436 (2021).

[43] T. Olsen, Theory and simulations of critical temperatures in CrI_3 and other 2D materials: Easy-axis magnetic order and easy-plane Kosterlitz Thouless transitions, MRS Commun. **9**, 1142 (2019).

[44] P. E. Blöchl, Projector augmented-wave method, Phys. Rev. B **50**, 17953 (1994).

[45] G. Kresse and D. Joubert, From ultrasoft pseudopotentials to the projector augmented-wave method, Phys. Rev. B **59**, 1758 (1999).

[46] G. Kresse and J. Furthmüller, Efficiency of *ab initio* total energy calculations for metals and semiconductors using a plane-wave basis set, Comput. Mater. Sci. **6**, 15 (1996).

[47] G. Kresse and J. Furthmüller, Efficient iterative schemes for *ab initio* total-energy calculations using a plane-wave basis set, Phys. Rev. B **54**, 11169 (1996).

[48] J. P. Perdew, K. Burke, and M. Ernzerhof, Generalized Gradient Approximation Made Simple, Phys. Rev. Lett. **77**, 3865 (1996).

[49] H. J. Monkhorst and J. D. Pack, Special points for Brillouin-zone integrations, Phys. Rev. B **13**, 5188 (1976).

[50] V. I. Anisimov, F. Aryasetiawan, and A. I. Lichtenstein, First-principles calculations of the electronic structure and spectra of strongly correlated systems: The LDA $+U$ method, J. Phys.: Condens. Matter **9**, 767 (1997).

[51] S. L. Dudarev, G. A. Botton, S. Y. Savrasov, C. J. Humphreys, and A. P. Sutton, Electron-energy-loss spectra and the structural stability of nickel oxide: An LSDA+U study, Phys. Rev. B **57**, 1505 (1998).

[52] M. Cococcioni and S. de Gironcoli, Linear response approach to the calculation of the effective interaction parameters in the LDA+U method, Phys. Rev. B **71**, 035105 (2005).

[53] A. Togo and I. Tanaka, First principles phonon calculations in materials science, Scr. Mater. **108**, 1 (2015).

[54] G. Henkelman, A. Arnaldsson, and H. Jónsson, A fast and robust algorithm for Bader decomposition of charge density, Comput. Mater. Sci. **36**, 354 (2006).

[55] W. Tang, E. Sanville, and G. Henkelman, A grid-based Bader analysis algorithm without lattice bias, J. Phys.: Condens. Matter **21**, 084204 (2009).

[56] E. Sanville, S. D. Kenny, R. Smith, and G. Henkelman, Improved grid-based algorithm for Bader charge allocation, J. Comput. Chem. **28**, 899 (2007).

[57] J. Liang, W. Wang, H. Du, A. Hallal, K. Garcia, M. Chshiev, A. Fert, and H. Yang, Very large Dzyaloshinskii-Moriya

interaction in two-dimensional Janus manganese dichalcogenides and its application to realize skyrmion states, Phys. Rev. B **101**, 184401 (2020).

[58] J. Yuan, Y. Yang, Y. Cai, Y. Wu, Y. Chen, X. Yan, and L. Shen, Intrinsic skyrmions in monolayer Janus magnets, Phys. Rev. B **101**, 094420 (2020).

[59] S. Zheng, C. Huang, T. Yu, M. Xu, S. Zhang, H. Xu, Y. Liu, E. Kan, Y. Wang, and G. Yang, High-temperature ferromagnetism in an Fe_3P monolayer with a large magnetic anisotropy, J. Phys. Chem. Lett. **10**, 2733 (2019).

[60] Q. Yang, X. Hu, X. Shen, A. V. Krasheninnikov, Z. Chen, and L. Sun, Enhancing ferromagnetism and tuning electronic properties of CrI_3 monolayers by adsorption of transition-metal atoms, ACS Appl. Mater. Interfaces **13**, 21593 (2021).

[61] K. Sheng, Z.-Y. Wang, H.-K. Yuan, and H. Chen, Two-dimensional hexagonal manganese carbide monolayer with intrinsic ferromagnetism and half-metallicity, New J. Phys. **22**, 103049 (2020).

[62] P. A. Maksimov, Z. Zhu, S. R. White, and A. L. Chernyshev, Anisotropic-Exchange Magnets on a Triangular Lattice: Spin Waves, Accidental Degeneracies, and Dual Spin Liquids, Phys. Rev. X **9**, 021017 (2019).

[63] N. Caci, L. Weber, and S. Wessel, Hierarchical single-ion anisotropies in spin-1 Heisenberg antiferromagnets on the honeycomb lattice, Phys. Rev. B **104**, 155139 (2021).

[64] T. Holstein and H. Primakoff, Field dependence of the intrinsic domain magnetization of a ferromagnet, Phys. Rev. **58**, 1098 (1940).

[65] M. Jaščur, *Quantum Theory of Magnetism* (Pavol Jozef Šafárik University in Košice, 2013).

[66] C. Timm, *Theory of Magnetism* (International Max Planck Research School for Dynamical Processes in Atoms, Molecules and Solids, 2015).

[67] Z. Xu and H. Zhu, Two-dimensional manganese nitride monolayer with room temperature rigid ferromagnetism under strain, J. Phys. Chem. C **122**, 14918 (2018).

[68] S.-S. Wang, Z.-M. Yu, Y. Liu, Y. Jiao, S. Guan, X.-L. Sheng, and S. A. Yang, Two-dimensional nodal-loop half-metal in monolayer MnN, Phys. Rev. Mater. **3**, 084201 (2019).

[69] See Supplemental Material at http://link.aps.org/supplemental/10.1103/PhysRevB.107.144409 for (i) calculation of Hubbard-U parameter by using linear response approximation and (ii) the dynamical and thermal stability of MnX monolayers.

[70] B. Wang, Y. Zhang, L. Ma, Q. Wu, Y. Guo, X. Zhang, and J. Wang, MnX (X = P, As) monolayers: A new type of two-dimensional intrinsic room temperature ferromagnetic half-metallic material with large magnetic anisotropy, Nanoscale **11**, 4204 (2019).

[71] A. Dahani, S. Kacimi, A. Boukortt, M. Bououdina, and A. Zaoui, DFT+U analysis of structural, electronic, and magnetic properties of Mn–As–Sb ternary systems, J. Supercond. Novel Magn. **27**, 2263 (2014).

[72] X. Chong, Y. Jiang, R. Zhou, and J. Feng, Pressure dependence of electronic structure and superconductivity of the MnX (X= N, P, As, Sb), Sci. Rep. **6**, 21821 (2016).

[73] R. Widita, S. Muhammady, R. D. Prasetiyawati, R. Marlina, L. Suryanegara, B. Purnama, R. Kurniadi, and Y. Darma, Revisiting the structural, electronic, and magnetic properties of (LaO)MnAs: Effect of Hubbard correction and origin of Mott-insulating behavior, ACS Omega **6**, 4440 (2021).

[74] E. Şaşıoğlu, I. Galanakis, C. Friedrich, and S. Blügel, *Ab initio* calculation of the effective on-site Coulomb interaction parameters for half-metallic magnets, Phys. Rev. B **88**, 134402 (2013).

[75] N. Si and T. Niu, Epitaxial growth of elemental 2D materials: What can we learn from the periodic table? Nano Today **30**, 100805 (2020).

[76] Y. Liu, E. S. Penev, and B. I. Yakobson, Probing the synthesis of two-dimensional boron by first-principles computations, Angew. Chem. Int. Ed. **52**, 3156 (2013).

[77] K. Iordanidou, M. Houssa, J. Kioseoglou, V. V. Afanas'ev, A. Stesmans, and C. Persson, Hole-doped 2D InSe for spintronic applications, ACS Appl. Nano Mater. **1**, 6656 (2018).

[78] P. Rosenzweig, H. Karakachian, D. Marchenko, K. Kuster, and U. Starke, Overdoping Graphene Beyond the van Hove Singularity, Phys. Rev. Lett. **125**, 176403 (2020).

[79] J. J. Quinn and K.-S. Yi, *Magnetic Ordering and Spin Waves, Solid State Physics: Principles and Modern Applications* (Springer International Publishing, Cham, 2018), pp. 281–320.

[80] M. Bloch, Magnon Renormalization in Ferromagnets Near the Curie Point, Phys. Rev. Lett. **9**, 286 (1962).